Volume 1
Number 1
February 2025
Pages 1-210

# EES Batteries

rsc.li/EESBatteries

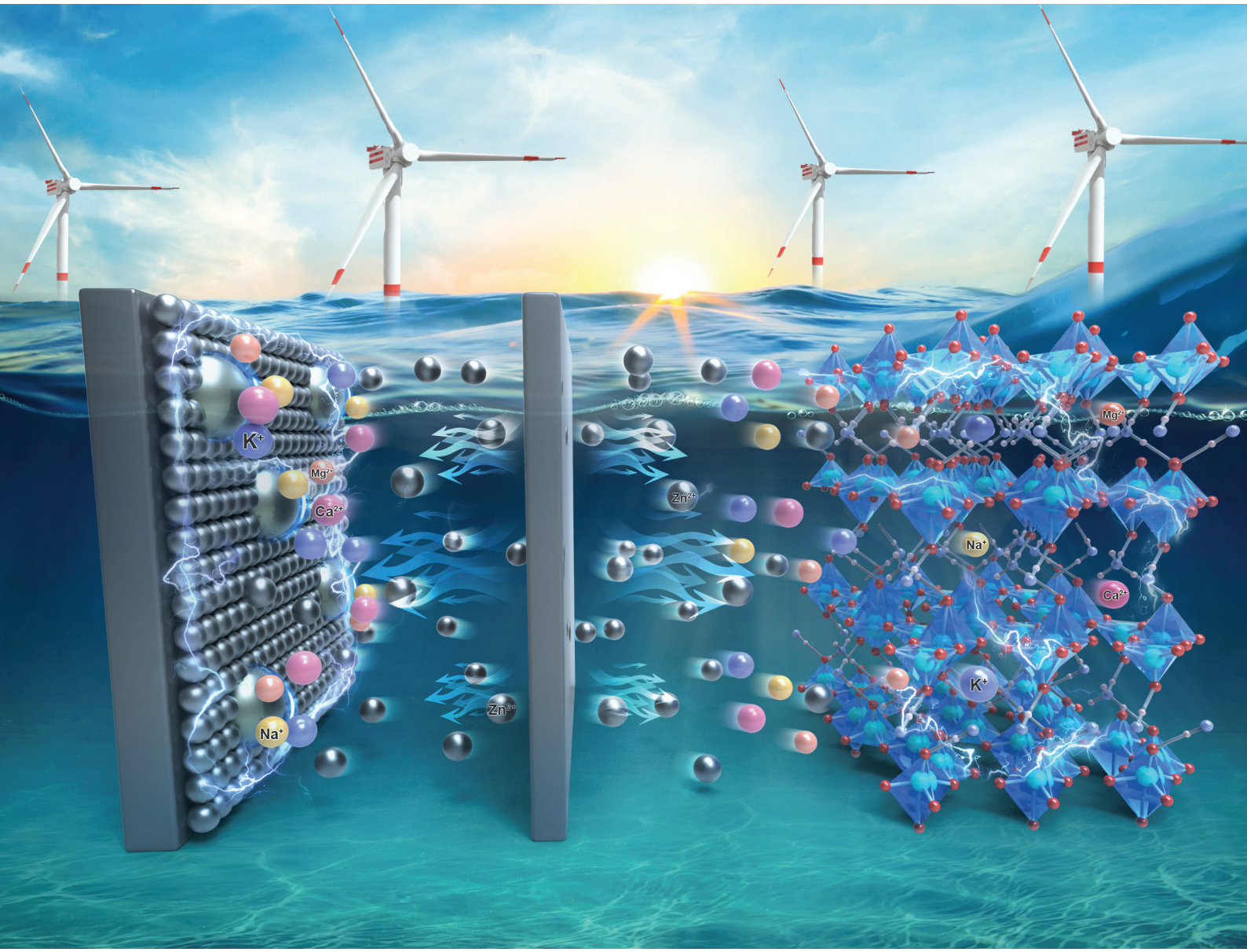


ISSN 3033-4071

ROYAL SOCIETY OF CHEMISTRY

**PAPER**
Xiaodong Shi, Xinlong Tian *et al.*
Natural seawater-based electrolytes for zinc-ion batteries

EES Batteries



PAPER

View Article Online
View Journal | View Issue



Cite this: *EES Batteries*, 2025, **1**, 161

# Natural seawater-based electrolytes for zinc-ion batteries†

Chuancong Zhou,‡[a] Zhenming Xu, ‡[b] Min Chen,‡[c] Qing Nan,[a] Jie Zhang,[a] Yating Gao,[a] Zejun Zhao,[a] Zhenyue Xing,[a] Jing Li,[a] Peng Rao,[a] Zhenye Kang, [a] Xiaodong Shi*[a] and Xinlong Tian *[a]

Designing high-entropy electrolytes is an effective strategy to promote the electrochemical performances of aqueous zinc-ion batteries (ZIBs). Seawater holds great potential as a natural solvent to configure high-entropy electrolytes due to its complex composition and high salinity. In this study, the electrochemical performances of the zinc anode and the $NH_4V_4O_{10}$ cathode reinforced by the seawater electrolyte have been comprehensively investigated. Theoretical calculations demonstrate that alkali metal cations ($Na^+$, $K^+$, $Mg^{2+}$, and $Ca^{2+}$) in the seawater electrolyte confer lower reduction potential and stronger adsorption energy for the zinc anode, which effectively inhibits dendrite growth through the electrostatic shielding effect. In addition, alkali metal cations also guarantee lower desolvation energy and stronger adsorption and insertion energy for the $NH_4V_4O_{10}$ cathode, which significantly improves the specific capacity through the preferential adsorption/insertion and additional (de)intercalation reactions of alkali metal cations. As expected, the corresponding Zn//Zn cells exhibit low voltage polarization and Zn//Cu cells present a high plating/stripping coulombic efficiency of 99.13%. Furthermore, Zn//$NH_4V_4O_{10}$ cells deliver a high capacity of 229.8 mA h $g^{-1}$ at 0.5 A $g^{-1}$ after 100 cycles and high cycling stability for 500 cycles at 2 A $g^{-1}$. These satisfactory results verify that the application of seawater electrolytes in ZIBs is practical.

Received 4th September 2024,
Accepted 14th October 2024

DOI: 10.1039/d4eb00002a

rsc.li/EESBatteries



**Broader context**

The practical applications of aqueous zinc-ion batteries (ZIBs) are severely restricted by the low utilization efficiency of the zinc metal anode and the low capacity of cathode materials. High-entropy electrolytes are a practical strategy to achieve dendrite-free zinc anodes and high-performance cathodes and can provide diverse solvation structures and rich interface chemistry. In this study, natural seawater is employed as the solvent to configure high-entropy electrolytes for ZIBs owing to the features of high ionic conductivity, rich salt composition and high salt concentration, and the electrochemical performances of the zinc metal anode and the $NH_4V_4O_{10}$ cathode reinforced by the seawater electrolyte are comprehensively investigated. As demonstrated by theoretical calculations and experimental data, the alkali metal cations ($Na^+$, $K^+$, $Mg^{2+}$, and $Ca^{2+}$) in the seawater electrolyte confer lower reduction potential and stronger adsorption energy for the zinc metal anode, effectively inhibiting dendrite growth through the electrostatic shielding effect. Meanwhile, these alkali metal cations also deliver lower desolvation energy and stronger adsorption as well as insertion energy for the $NH_4V_4O_{10}$ cathode, significantly improving the specific capacity through the preferential adsorption/insertion behavior and the additional (de)intercalation of alkali metal cations. This work will drive the comprehensive utilization of seawater resources, get rid of the urgent dependence on ultra-pure water, and facilitate the development of seawater-based secondary batteries.

[a]*School of Chemistry and Chemical Engineering, School of Marine Science and Engineering, State Key Laboratory of Marine Resource Utilization in South China Sea, Hainan University, Haikou 570228, China. E-mail: shixiaodong@hainanu.edu.cn, tianxl@hainanu.edu.cn*

[b]*College of Materials Science and Technology, Nanjing University of Aeronautics and Astronautics, Nanjing 210016, China*

[c]*School of Materials Science and Engineering, Dongguan University of Technology, Dongguan 523808, China*

† Electronic supplementary information (ESI) available. See DOI: https://doi.org/10.1039/d4eb00002a

‡ Co-first authors: these authors contributed equally.

## 1. Introduction

Zinc-ion batteries (ZIBs) have the advantages of high safety, ease of manufacture, and low cost and hold great application potential for large-scale energy storage systems.[1–4] However, the practical applications of ZIBs are severely restricted by the low utilization efficiency of the zinc metal anode and the unsatisfactory specific capacity of cathode materials. Electrolyte optimization is an effective approach to simultaneously realize a dendrite-free zinc anode and a high-performance cathode for ZIBs,[5–7] including "salt-in-water" electrolytes,[8] inorganic colloidal electrolytes,[9] gel electrolytes,[10] and solid-state electrolytes.[11,12] Unfortunately, these electrolytes always face a trade-off dilemma between the cost and performance of ZIBs,[13,14] and it is still a challenge to develop new electrolytes to meet the economic and practical requirements.[15–17]

As an emerging hotspot in rechargeable battery research,[18–22] high-entropy electrolytes provide diverse solvation structures and rich interface chemistry, which can widen the electrochemically stable voltage and temperature window,[23] enhance the ionic conductivity,[24] and achieve a stable solid electrolyte interface,[21,22,25] thereby boosting the battery performance.[26] A mixed $ZnCl_2$ and LiCl electrolyte with a high-entropy solvation structure ($Li_2ZnCl_4{\cdot}9H_2O$) reportedly yielded a high plating/stripping coulombic efficiency (CE) of the zinc anode of 100% and a wide operating temperature range of zinc–air batteries from −60 to 80 °C.[27] In addition, a 5 M $Zn(ClO_4)_2$ electrolyte effectively increased the tetrahedral entropy of water molecules and reduced the freezing point of an aqueous electrolyte to −80 °C.[28] Therefore, the development of high-entropy electrolytes with suitable solutes and solvents is crucial for the design of high-performance ZIBs.

With the features of high ionic conductivity, rich salt composition, and high salinity, seawater is a promising natural solvent for configuring high-entropy electrolytes for ZIBs.[29,30] Firstly, inorganic salts containing alkali metal ions, such as LiCl,[31] $Na_2SO_4$,[32] and $MgSO_4$,[33] can be used as electrolyte additives to guide uniform zinc deposition through the electrostatic shielding effect, because alkali metal cations have a lower reduction potential and stronger adsorption energy than $Zn^{2+}$ ions.[34–37] Secondly, alkali metal cations in the seawater electrolyte favor additional (de)intercalation reactions during the cycling process,[38–40] thus promoting the specific capacity of cathode materials.[41,42]

In this study, natural seawater was employed as a solvent to configure high-entropy electrolytes for ZIBs, and its positive effects on both the zinc metal anode and the $NH_4V_4O_{10}$ cathode were analyzed. Alkali metal cations lead to a lower reduction potential and stronger adsorption energy compared to $Zn^{2+}$ ions for the zinc metal anode, which can act as an electrostatic shield layer to suppress dendrite growth and guarantee a reversible interfacial reaction. Notably, Zn//Zn cells in the seawater electrolyte exhibit a stable cycling performance at 5 mA $cm^{-2}$ and a high $Zn^{2+}$ transference number of 0.44, whereas Zn//Cu cells in the seawater electrolyte exhibit a high plating/stripping CE of 99.13% at 2 mA $cm^{-2}$. In addition, alkali metal cations in the seawater electrolyte deliver lower desolvation energy and stronger adsorption and insertion energies for the $NH_4V_4O_{10}$ cathode, which can facilitate the (de)intercalation reaction and improve the specific capacity. Benefiting from these merits, Zn//$NH_4V_4O_{10}$ cells in the seawater electrolyte achieve a high capacity of 229.8 mA h $g^{-1}$ after 100 cycles at 0.5 A $g^{-1}$ and 200.7 mA h $g^{-1}$ after 500 cycles at 2 A $g^{-1}$, manifesting the "killing two birds with one stone" effect of the seawater electrolyte on the practical application of ZIBs.

## 2. Results and discussion

Alkali metal cations in the seawater of the South China Sea were analyzed using an inductively coupled plasma (ICP) spectrometer. The molar concentrations of $Na^+$, $K^+$, $Ca^{2+}$, and $Mg^{2+}$ ions in the seawater were determined as 0.47, 0.016, 0.018, and 0.056 M, respectively (Table S1†). The optimal content of $ZnSO_4$ in the seawater electrolyte was confirmed by a gradient contrast experiment. Fig. S1a and b† show that the 1.88 M $ZnSO_4$–seawater electrolyte (marked as $ZnSO_4$–seawater electrolyte) yields the smallest voltage polarization in Zn//Zn cells and the highest capacity in Zn//$NH_4V_4O_{10}$ cells. Additionally, the cycling performances of $Na_{0.33}V_2O_5$, $NaV_3O_8$, and $NH_4V_4O_{10}$ cathodes in the $ZnSO_4$–seawater electrolyte have been compared in Fig. S1c,† verifying the high capacity of the $NH_4V_4O_{10}$ cathode.

To reveal the advantages of the seawater electrolyte, 1.88 M $ZnSO_4$ electrolyte was configured with ultrapure water as the solvent and served as a contrast sample (labeled as $ZnSO_4$ electrolyte). Fig. 1a schematically illustrates that the $Zn^{2+}$ ions in the $ZnSO_4$ electrolyte exhibit an uneven deposition behavior and disordered dendrite growth due to the tip effect and interfacial side reactions. Owing to the electrostatic shielding effect, alkali metal cations in the $ZnSO_4$–seawater electrolyte preferentially reach the tip or low-lying position of the zinc metal (Fig. 1b), cover the deposition interface, and act as an electrostatic shield layer to guide uniform zinc deposition, thereby guaranteeing a dendrite-free zinc anode.[33,34] Density functional theory (DFT) calculations were also performed to reveal the action mechanism and evaluate the adsorption energy of alkali metal cations on the surface of the zinc metal (Fig. 1c). Notably, the adsorption energies of $Na^+$, $K^+$, $Ca^{2+}$, and $Mg^{2+}$ ions are −1.81, −2.07, −1.97, and −0.71 eV, respectively, much stronger than that of $Zn^{2+}$ ions (−0.44 eV), implying that alkali metal cations in seawater can be preferentially adsorbed on the surface of the zinc metal. Fig. S2† presents the charge transfer impedances of Zn//Zn cells at different temperatures (30–70 °C) in different electrolytes. Combined with the Arrhenius equation (eqn (S1) and (S2)†), the corresponding activation energy barriers in the $ZnSO_4$–seawater and $ZnSO_4$ electrolytes were calculated as 27.43 and 37.49 kJ $mol^{-1}$, respectively, manifesting the fast interfacial reaction kinetics of Zn//Zn cells in the $ZnSO_4$–seawater electrolyte.[43]

Fig. S3† presents the current–time curves and electrochemical impedance spectroscopy (EIS) data of Zn//Zn cells before and after the activation process. Based on eqn (S3) and Table S2,† the $Zn^{2+}$ transference numbers of Zn//Zn cells in the

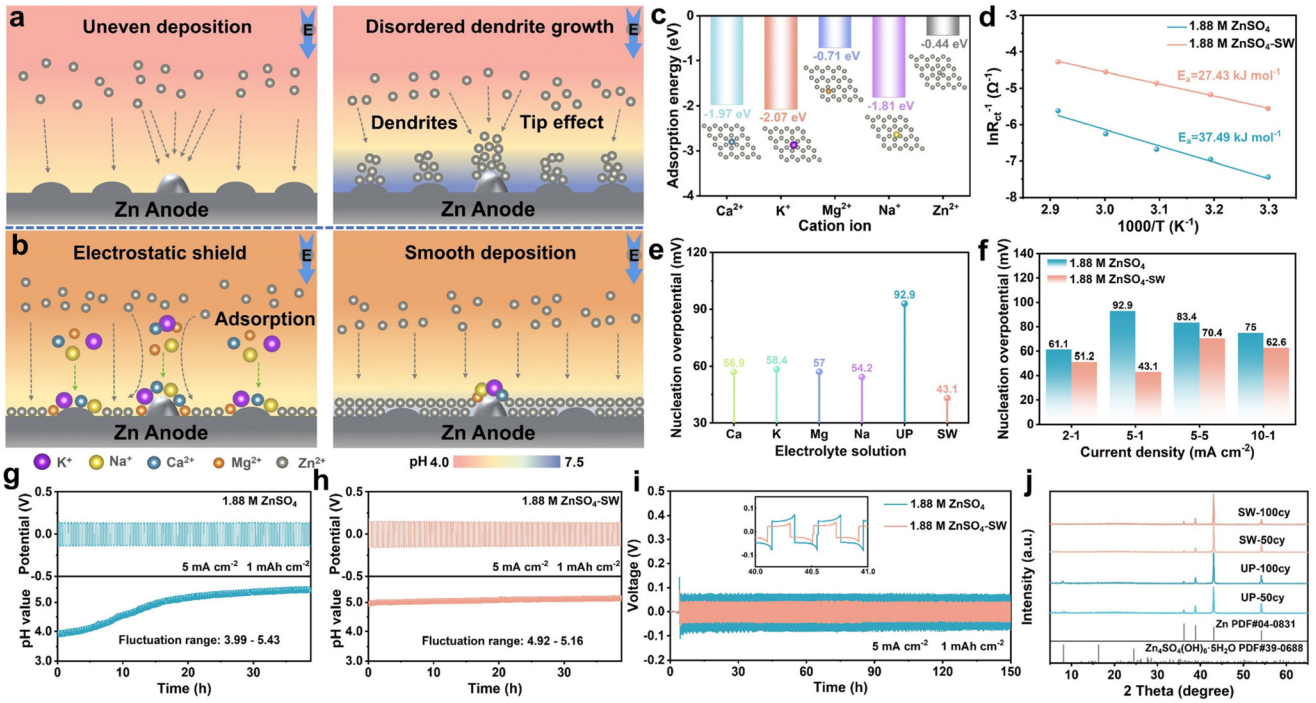


**Fig. 1** Schematic illustration of zinc deposition in (a) $ZnSO_4$ and (b) $ZnSO_4$–seawater electrolytes; (c) adsorption energy of $Na^+$, $K^+$, $Ca^{2+}$, $Mg^{2+}$, and $Zn^{2+}$ ions on the surface of the zinc metal; (d) interfacial activation energy barrier of Zn//Zn cells in $ZnSO_4$ and $ZnSO_4$–seawater electrolytes; (e) comparison of the nucleation overpotentials of Zn//Zn cells in $ZnSO_4$, $ZnSO_4$–seawater, 1.88 M $ZnSO_4$–0.47 M NaCl, 1.88 M $ZnSO_4$–0.016 M KCl, 1.88 M $ZnSO_4$–0.018 M $CaCl_2$, and 1.88 M $ZnSO_4$–0.056 M $MgCl_2$ electrolytes under the conditions of 5 mA $cm^{-2}$–1 mA h $cm^{-2}$; (f) the nucleation overpotentials of Zn//Zn cells in $ZnSO_4$ and $ZnSO_4$–seawater electrolytes under different conditions; *in situ* pH changes of Zn//Zn cells during the cycling process in (g) $ZnSO_4$ and (h) $ZnSO_4$–seawater electrolytes; (i) galvanostatic cycling performance of Zn//Zn cells in $ZnSO_4$ and $ZnSO_4$–seawater electrolytes under the conditions of 5 mA $cm^{-2}$–1 mA h $cm^{-2}$; (j) XRD patterns of zinc foil in Zn//Zn cells after 50 and 100 cycles in $ZnSO_4$ and $ZnSO_4$–seawater electrolytes.

$ZnSO_4$–seawater and $ZnSO_4$ electrolytes are 0.44 and 0.36, respectively, proving the enhanced transport behavior of $Zn^{2+}$ ions.[44] These results verify that the $ZnSO_4$–seawater electrolyte with high-entropy characteristics effectively facilitates zinc deposition, accelerates charge transfer and zinc ion transport, stabilizes the interfacial reaction environment, reduces the activation energy, and strengthens the interfacial reaction kinetics between the zinc anode and electrolyte.[45–47] Additionally, the dynamic contact angle test demonstrates that the $ZnSO_4$–seawater electrolyte has a better surface wettability with Zn foil (Fig. S4a†), favoring the construction of a stable solid–liquid contact interface.[48] As expected, Zn//Zn cells in the $ZnSO_4$–seawater electrolyte have a charge transfer impedance of 400 Ω, which is smaller than that of the $ZnSO_4$ electrolyte (480 Ω), indicating the enhanced charge transfer kinetics in the seawater electrolyte (Fig. S4b†). Table S3† shows that the ionic conductivity of the $ZnSO_4$–seawater electrolyte is 13.8 mS $cm^{-1}$, which is higher than that of the $ZnSO_4$ electrolyte (13.0 mS $cm^{-1}$) because the seawater has a higher ionic conductivity than ultrapure water (Fig. S4c and d†).[41] The cycling performances of Zn//Zn cells in 1.88 M $ZnSO_4$–0.47 M NaCl electrolyte, 1.88 M $ZnSO_4$–0.016 M KCl electrolyte, 1.88 M $ZnSO_4$–0.018 M $CaCl_2$ electrolyte, and 1.88 M $ZnSO_4$–0.056 M $MgCl_2$ electrolyte were tested to study the effects of individual alkali metal cations in seawater on the nucleation overpotentials (Fig. S5†). As a result, the nucleation overpotentials of Zn// Zn cells in $Na^+$-, $Ca^{2+}$-, $Mg^{2+}$-, and $K^+$-containing electrolytes (Fig. 1e) are 54.2, 56.9, 57, and 58.4 mV at 5 mA $cm^{-2}$–1 mA h $cm^{-2}$, respectively, which are much smaller than that in the $ZnSO_4$ electrolyte (92.9 eV), demonstrating that the alkali metal cations in seawater are conducive to reducing the zinc nucleation barriers. The corresponding nucleation overpotentials (Fig. 1f and S6†) in the $ZnSO_4$–seawater electrolyte under the conditions of 2 mA $cm^{-2}$–1 mA h $cm^{-2}$, 5 mA $cm^{-2}$–1 mA h $cm^{-2}$, 5 mA $cm^{-2}$–5 mA h $cm^{-2}$, and 10 mA $cm^{-2}$–1 mA h $cm^{-2}$ are 51.2, 43.1, 70.4, and 62.6 mV, respectively, which are smaller than those in the $ZnSO_4$ electrolyte, indicating that the seawater reduces the zinc nucleation overpotential.[49,50]

The pH changes in Zn//Zn cells in the different electrolytes during the cycling process were monitored with an *in situ* pH meter (Fig. 1g and h). The $ZnSO_4$–seawater electrolyte displays a smooth pH change from 4.92 to 5.16, indicating a stable interfacial reaction environment.[51] In contrast, the pH values in the $ZnSO_4$ electrolyte increase from 3.99 to 5.43, which can be ascribed to the undesirable side reactions between the zinc metal anode and the liquid electrolyte. Benefitting from the above merits, Zn//Zn cells in the $ZnSO_4$–seawater electrolyte exhibit more stable and smaller voltage polarization under different test conditions (Fig. 1i and S7†), while the shelving-recovery performance and rate performance (Fig. S8†) of Zn//

Zn cells were also satisfactory, implying reversible and stable zinc deposition behavior in the $ZnSO_4$–seawater electrolyte. Moreover, X-ray diffraction (XRD) patterns and SEM images of Zn foil in Zn//Zn cells were investigated to reveal the performance differences in different electrolytes. Notably, the characteristic peaks of $Zn_4SO_4(OH)_6{\cdot}5H_2O$ are detectable on the surface of zinc foil in the $ZnSO_4$ electrolyte after 50 and 100 cycles, whereas no byproducts can be observed in the $ZnSO_4$–seawater electrolyte (Fig. 1j), suggesting that seawater plays an active role in inhibiting the formation of byproducts. This phenomenon can be observed in the *in situ* optical microscopy images (Fig. S9†), confirming the positive effects of dendrite inhibition and interface stabilization on the zinc anode in the $ZnSO_4$–seawater electrolyte.[52,53] In addition, the Zn foil in the $ZnSO_4$–seawater electrolyte provides a dendrite-free surface, much cleaner than that in the $ZnSO_4$ electrolyte (Fig. S10†).

Fig. S11a† shows the CV curves of Zn//Cu cells in different electrolytes. Notably, the $ZnSO_4$–seawater electrolyte yields a wider redox peak current range of −68.34 to 71.54 mA (*vs.* −51.19 to 58.79 mA of the $ZnSO_4$ electrolyte), suggesting an enlarged electrochemical active area and more active nucleation sites. In addition, the $ZnSO_4$–seawater electrolyte has a lower zinc deposition potential of −0.0618 V (*vs.* −0.074 V of the $ZnSO_4$ electrolyte), manifesting a reduced zinc nucleation barrier, which can be confirmed by the galvanostatic charge/discharge curves (Fig. S11b and c†) and nucleation overpotential profiles of Zn//Cu cells (Fig. S11d and S12†). Fig. S11e† indicates that the nucleation overpotential in the $ZnSO_4$–seawater electrolyte is 22.2, 17, and 24.2 mV at 2 mA $cm^{-2}$–1 mA h $cm^{-2}$, 2 mA $cm^{-2}$–2 mA h $cm^{-2}$, and 5 mA $cm^{-2}$–1 mA h $cm^{-2}$, respectively, which are much smaller than those in the $ZnSO_4$ electrolyte. In general, a small nucleation overpotential is conducive to reversible Zn plating/stripping on the surface of Cu foil. Therefore, the $ZnSO_4$–seawater electrolyte yields a more stable plating/stripping CE than the $ZnSO_4$ electrolyte, and the average CE is 99.13% at 2 mA $cm^{-2}$–1 mA h $cm^{-2}$ after 100 cycles (Fig. S11f†). The nucleation overpotentials of Zn//Cu cells in $Na^+$-, $Ca^{2+}$-, $Mg^{2+}$-, and $K^+$-containing electrolytes (Fig. S11g and S13†) are 31.6, 39.2, 37.6, and 41.1 mV at 2 mA $cm^{-2}$–1 mA h $cm^{-2}$, respectively, much smaller than that of the $ZnSO_4$ electrolyte (60.6 eV), further confirming that alkali metal cations in seawater contribute to the reduction of the zinc nucleation barrier.[54] In addition, the SEM images of the Cu foil in Zn//Cu cells were characterized after ten cycles in different electrolytes. The Cu foil in the $ZnSO_4$–seawater electrolyte has a smoother and cleaner surface (Fig. S11h and i†), indicating highly reversible Zn plating/stripping behavior without notable attachment of by-products.

Zn//$NH_4V_4O_{10}$ cells were assembled and investigated in different electrolytes with Zn foil and homemade $NH_4V_4O_{10}$ as the anode and cathode, respectively. The CV curves reveal the differences in the Zn storage behavior of the $NH_4V_4O_{10}$ cathode. The normalized CV curves of the $NH_4V_4O_{10}$ cathode in the $ZnSO_4$–seawater electrolyte have a larger enclosed area and more redox peaks than those of the $ZnSO_4$ electrolyte (Fig. 2a and b), indicating a higher energy density and a complex reaction mechanism of Zn//$NH_4V_4O_{10}$ cells in the $ZnSO_4$–seawater electrolyte, which may be ascribed to the additional (de)intercalation of alkali metal cations ($Na^+$, $Ca^{2+}$, $Mg^{2+}$, $K^+$) in the seawater during the cycling process. The CV curves of Zn//$NH_4V_4O_{10}$ cells with natural seawater as the electrolyte (Fig. S14†) also show typical redox peaks belonging to the (de)intercalation reactions of layered vanadium-based oxides. Two reduction peaks at 0.595 and 0.325 V and two oxidation peaks at 0.776 and 0.911 V were detected in the first scan, confirming the (de)intercalation reaction of alkali metal cations in seawater. In the second and third scans, the primary oxidation peak is shifted to 0.67 and 0.687 V, respectively, implying a change in the crystal structure of $NH_4V_4O_{10}$ after the (de)intercalation of the alkali metal cations. To further demonstrate the capacity contribution of alkali metal cations in seawater, the specific capacities of the $NH_4V_4O_{10}$ cathode in the electrolytes of seawater, ultrapure water, 0.47 M NaCl solution, 0.016 M KCl solution, 0.018 M $CaCl_2$ solution, and 0.056 M $MgCl_2$ solution were tested at 500 mA $g^{-1}$ (Fig. S15†). The $NH_4V_4O_{10}$ cathode has no capacity in ultrapure water but has the highest capacity in seawater. The specific capacity of the $Na^+$-, $Ca^{2+}$-, $Mg^{2+}$-, and $K^+$-containing solutions is proportional to the molar concentration of the metal cations, and the specific capacity in seawater can be regarded as capacity superposition of individual cation solutions. Galvanostatic charge/discharge profiles of Zn//$NH_4V_4O_{10}$ cells in different electrolytes at 500 mA $g^{-1}$ are compared in Fig. 2c. As expected, the initial specific capacity of the $NH_4V_4O_{10}$ cathode in the $ZnSO_4$–seawater electrolyte is higher than that in the $ZnSO_4$ electrolyte, and the voltage plateaus correspond to the redox peaks in the CV curves. The charge transfer resistance of the $NH_4V_4O_{10}$ cathode after cyclic activation in the $ZnSO_4$–seawater electrolyte is lower than that in the $ZnSO_4$ electrolyte (Fig. 2d), verifying the lower interfacial charge transfer energy barrier.

Furthermore, the cycling performances of the $NH_4V_4O_{10}$ cathode at 500 mA $g^{-1}$ in different electrolytes were compared. The $NH_4V_4O_{10}$ cathode exhibits a highly reversible capacity of 229.8 mA h $g^{-1}$ after 100 cycles in the $ZnSO_4$–seawater electrolyte (Fig. 2e). The corresponding capacity retention ratio is 72.2%, which is higher than that of the $ZnSO_4$ electrolyte. As shown in Fig. S16a,† the Zn//$NH_4V_4O_{10}$ batteries in the $ZnSO_4$–seawater electrolyte deliver a high capacity of 225.97 mA h $g^{-1}$ and a high coulombic efficiency (CE) of 80.7% after two continuous self-discharge cycles. Under the same test conditions, the Zn//$NH_4V_4O_{10}$ batteries in the $ZnSO_4$ electrolyte only maintain a low capacity of 114.66 mA h $g^{-1}$ and a low CE of 68.8% (Fig. S16b†), implying inferior resistance to self-discharge behavior. Fig. 2f shows the rate capabilities of the $NH_4V_4O_{10}$ cathodes in different electrolytes. Notably, the reversible capacity of the $ZnSO_4$–seawater electrolyte is 342.4, 304.2, 275.1, 253.2, and 209.3 mA h $g^{-1}$ at 200, 500, 1000, 2000, and 5000 mA $g^{-1}$, respectively. These values are higher than the corresponding capacities of the $ZnSO_4$ electrolyte due to the higher ionic conductivity and additional intercalation reactions of metal cations in seawater. The long-term cycling stability of the $NH_4V_4O_{10}$ cathode in different electrolytes was verified at 2000 mA $g^{-1}$. The specific capacity of $NH_4V_4O_{10}$ in the

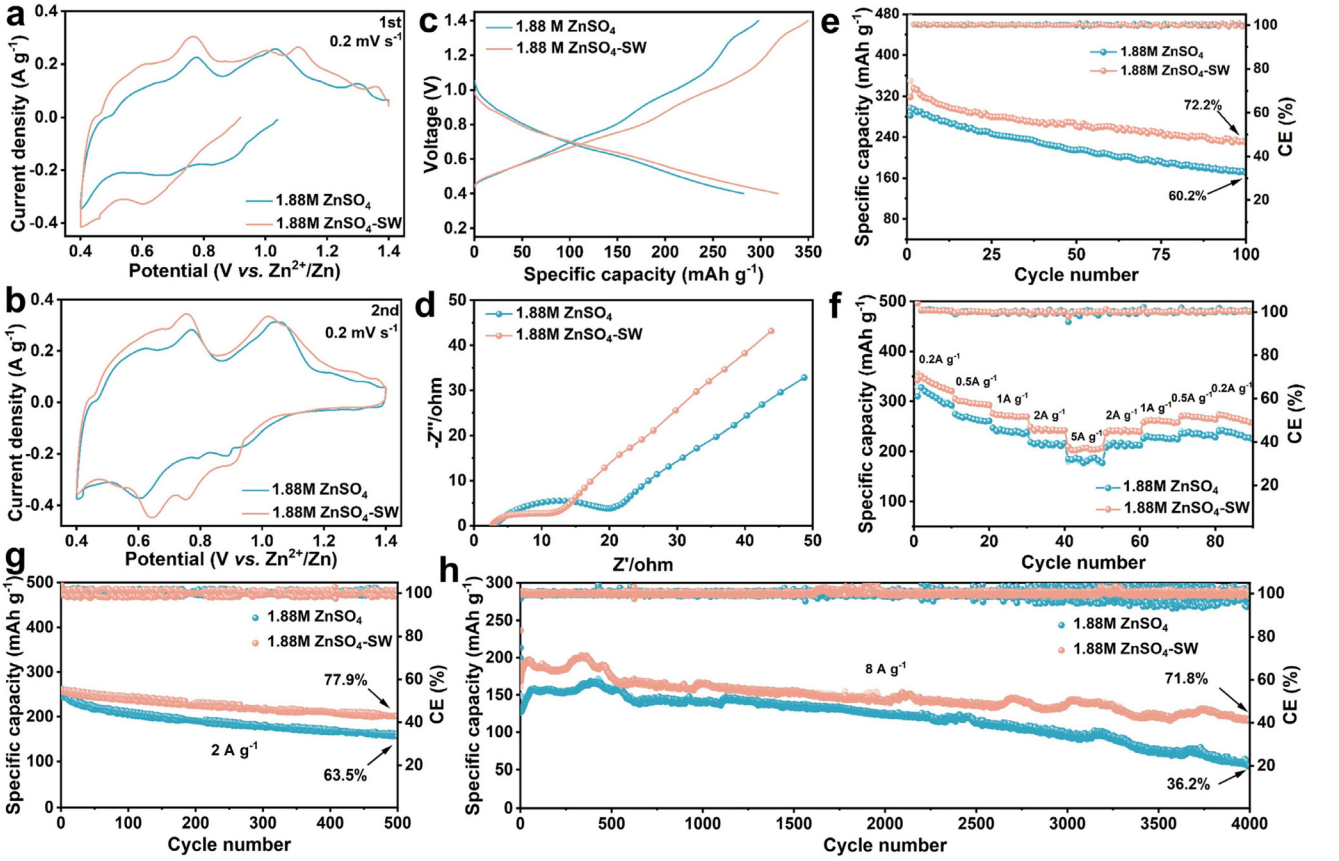


Fig. 2 Comparison of (a and b) CV curves, (c) galvanostatic charge/discharge curves, and (d) EIS of the $NH_4V_4O_{10}$ cathode in different electrolytes; (e) cycling performance of the $NH_4V_4O_{10}$ cathode in different electrolytes at 500 mA $g^{-1}$; (f) rate capability of the $NH_4V_4O_{10}$ cathode in different electrolytes at current densities of 200, 500, 1000, 2000, and 5000 mA $g^{-1}$; long-term cycling stability of the $NH_4V_4O_{10}$ cathode in different electrolytes at (g) 2000 mA $g^{-1}$ and (h) 8000 mA $g^{-1}$.

$ZnSO_4$–seawater electrolyte decreases from 257.6 to 200.7 mA h $g^{-1}$ during 500 cycles, with a high retention ratio of 77.9% (Fig. 2g). In contrast, the reversible capacity of the $ZnSO_4$ electrolyte stabilizes at 155.4 mA h $g^{-1}$. Moreover, the $NH_4V_4O_{10}$ cathode in the $ZnSO_4$–seawater electrolyte delivers a high reversible capacity of 115 mA h $g^{-1}$ after 4000 cycles at 8 A $g^{-1}$ with a high retention ratio of 71.8% (Fig. 2h), which is far higher than that in the $ZnSO_4$ electrolyte, manifesting the superior structural stability and wide operating current range of the $NH_4V_4O_{10}$ cathode in the $ZnSO_4$–seawater electrolyte. Additionally, XRD patterns and SEM images of Zn foil in Zn//$NH_4V_4O_{10}$ cells after 10 cycles in different electrolytes were collected (Fig. S17†), in which the Zn foil in the $ZnSO_4$–seawater electrolyte maintains a dendrite-free and clean surface owing to the electrostatic shielding effect induced by the alkali metal cations in seawater.

*In situ* pH changes of the Zn//$NH_4V_4O_{10}$ cells in different electrolytes during the cycling process were also measured (Fig. 3a, b and S18†). The pH of the Zn//$NH_4V_4O_{10}$ cells in the $ZnSO_4$–seawater electrolyte ranges from 4.96 to 5.07, whereas that of the $ZnSO_4$ electrolyte increases from 4.13 to 5.09, demonstrating a stable solid–liquid interface reaction environment for both the $NH_4V_4O_{10}$ cathode and the zinc anode in the seawater electrolyte. Furthermore, the CV curves at different scan rates (0.2–1.0 mV $s^{-1}$) and the corresponding *b* values of the redox peaks of the $NH_4V_4O_{10}$ cathode in the $ZnSO_4$–seawater and $ZnSO_4$ electrolytes were analyzed to determine the energy storage reaction types. Three pairs of redox peaks were observed (Fig. S19a and S20a†), which are consistent with the (de)intercalation reactions of the metal cations in the crystalline structure of $NH_4V_4O_{10}$. Based on eqn (S4) and (S5),† the *b* values corresponding to the redox peaks of the $NH_4V_4O_{10}$ cathode in both the $ZnSO_4$–seawater electrolyte (Fig. S19b†) and the $ZnSO_4$ electrolyte (Fig. S20b†) are relatively close to 1, indicating that the cation storage behavior is controlled by the adsorption reaction mechanism. Based on eqn (S6) and (S7),† the pseudocapacitive contribution ratio can be quantitatively calculated. As summarized in Fig. S19c and d,† the pseudocapacitive contribution ratios of Zn//$NH_4V_4O_{10}$ cells in the $ZnSO_4$–seawater electrolyte are 72%, 74.6%, 78.2%, 81.7%, and 85.2% at 0.2, 0.4, 0.6, 0.8, and 1.0 mV $s^{-1}$, respectively, which are higher than the corresponding values (48.8%/63.2%/67.5%/70.7%/75.7%) in the $ZnSO_4$ electrolyte (Fig. S20c and d†). The considerable pseudocapacitive adsorption capability of the $NH_4V_4O_{10}$ cathode can be attributed to the strong adsorption behavior between $NH_4V_4O_{10}$ and $Na^+$, $Ca^{2+}$, $Mg^{2+}$,

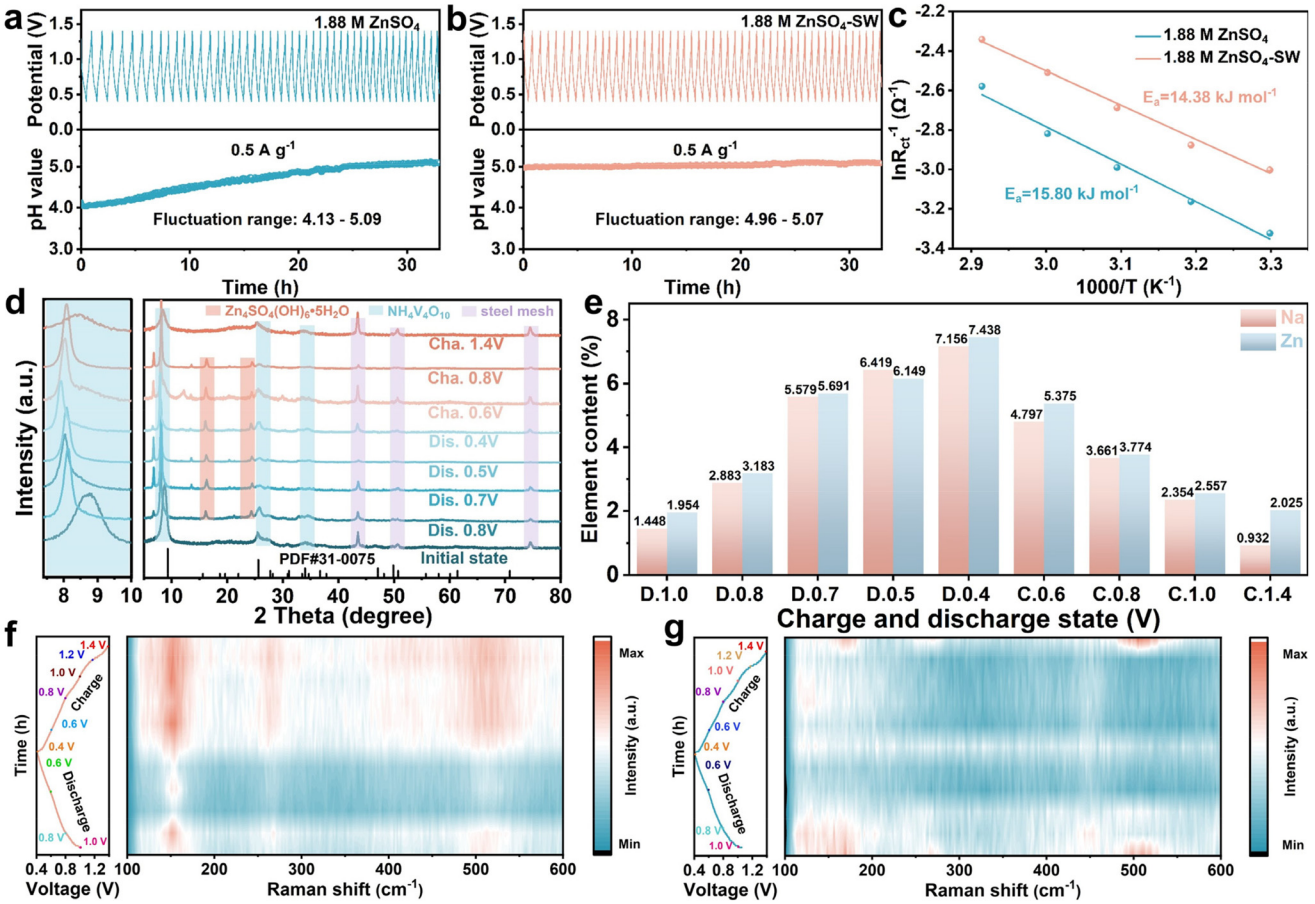


Fig. 3 *In situ* pH test of Zn//$NH_4V_4O_{10}$ cells during cycling in (a) $ZnSO_4$ and (b) $ZnSO_4$–seawater electrolytes; (c) interfacial activation energy of the $NH_4V_4O_{10}$ cathode in different electrolytes; (d) XRD patterns of the $NH_4V_4O_{10}$ cathode in the $ZnSO_4$–seawater electrolyte at different charge and discharge states; (e) Na/Zn element content of the $NH_4V_4O_{10}$ cathode in the $ZnSO_4$–seawater electrolyte at different charge and discharge states measured by ICP; *in situ* Raman spectra of the $NH_4V_4O_{10}$ cathode during cycling in (f) $ZnSO_4$–seawater and (g) $ZnSO_4$ electrolytes.

$K^+$, and $Zn^{2+}$ ions in the $ZnSO_4$–seawater electrolyte.[55,56] Fig. S21a and b† displays the Nyquist plots of Zn//$NH_4V_4O_{10}$ cells in the $ZnSO_4$–seawater and $ZnSO_4$ electrolytes at different temperatures (30–70 °C), respectively. According to the Arrhenius equation, the interfacial activation energy of $NH_4V_4O_{10}$ (Fig. 3c) in the $ZnSO_4$–seawater and $ZnSO_4$ electrolytes was calculated to be 14.38 and 15.8 kJ $mol^{-1}$, respectively. The lower activation energy of the $ZnSO_4$–seawater electrolyte indicates accelerated reaction kinetics at the solid–liquid interface of the $NH_4V_4O_{10}$ cathode.

The $NH_4V_4O_{10}$ cathode was prepared by a hydrothermal method[57] and characterized by XRD and X-ray photoelectron spectroscopy (XPS) (Fig. S22†). The characteristic (001) and (110) peaks of $NH_4V_4O_{10}$ were located at 9.2° and 25.5°, respectively, which agree with the peak locations in the standard material card (PDF#31-0075). Furthermore, the crystal structure of $NH_4V_4O_{10}$ is orderly layered with connected [$VO_6$] polyhedra and embedded ammonium ions. The initial V 2p spectra demonstrate that the mixed chemical valence states of vanadium in $NH_4V_4O_{10}$ are dominated by $V^{5+}$ and $V^{4+}$. Different characterization techniques were adopted to reveal the energy-storage mechanism of the $NH_4V_4O_{10}$ cathode in the $ZnSO_4$–seawater electrolyte. XRD patterns (Fig. 3d) corresponding to different charge and discharge states confirm the regular shift of the characteristic (001) and (110) peaks during the cycling process. The characteristic peaks shift to a lower diffraction angle with an increase in the discharge depth, indicating an enlarged lattice spacing based on the Bragg equation. A similar phenomenon was observed for the O 1s and Zn 2p spectra of the $NH_4V_4O_{10}$ cathode (Fig. S23†). These results can be explained by the intercalation of $Zn^{2+}$ ions and alkali metal cations ($Na^+$, $Ca^{2+}$, $Mg^{2+}$, and $K^+$) in the layered structure, which effectively expands the lattice spacing of $NH_4V_4O_{10}$. During the charging process, the characteristic peaks shift back to higher diffraction angles, corresponding to the deintercalation of $Zn^{2+}$ ions and alkali metal cations from the layered structure of $NH_4V_4O_{10}$. Compared with the initial state, slight peak location differences in the fully charged state can be ascribed to residual intercalated $Zn^{2+}$ ions and alkali metal cations. Furthermore, the (de)intercalation behavior of $Na^+$ ions is adequately demonstrated by the fitted Na 1s spectra of $NH_4V_4O_{10}$ in different charge and discharge states (Fig. S24†), which show the highest intensity in the fully discharged state and the lowest intensity in the fully charged

state, suggesting the reversible insertion and extraction of $Na^+$ ions during cycling.

The (de)intercalation reactions of $Zn^{2+}$ ions and alkali metal cations can also be directly verified by valence changes in V, which is the only variable element in $NH_4V_4O_{10}$. The $V^{5+}$ and $V^{4+}$ regions decrease and increase with increasing discharge depth, respectively, compared with the initial state (Fig. S25a and b†), confirming that the intercalation of $Zn^{2+}$ ions and alkali metal cations reduces the valence state of vanadium. Opposite valence region changes of V can be detected during the charging process (Fig. S25c and d†), which can be attributed to the deintercalation of $Zn^{2+}$ ions and alkali metal cations. In addition, the (de)intercalation reaction was verified by recording the changes in the Na/Zn content of the $NH_4V_4O_{10}$ cathode at different charge and discharge states. Based on the ICP test (Fig. 3e), the Na/Zn content increases and reaches its peak value in the fully discharged state, further verifying the insertion of $Zn^{2+}$ and $Na^+$ ions into $NH_4V_4O_{10}$ as well as the results obtained from element mapping images (Fig. S26†). Additionally, *in situ* Raman spectra of the $NH_4V_4O_{10}$ cathode in different electrolytes were measured to uncover the differences in structure evolution during the cycling process. For the $ZnSO_4$–seawater electrolyte (Fig. 3f), the regular signals around 150, 260, and 500 $cm^{-1}$ are well corresponding to the bending vibrations of $\delta$(–O–V–O–V–), $\delta$(V═O), and the stretching vibration of $\nu$(V–O), respectively, manifesting the relatively reversible crystal structure of the $NH_4V_4O_{10}$ cathode. The XRD pattern of the $NH_4V_4O_{10}$ cathode after 30 cycles also proves its stable crystal structure in the $ZnSO_4$–seawater electrolyte during the cycling process (Fig. S27†). In contrast, the characteristic signals of $NH_4V_4O_{10}$ are chaotic and disordered in the $ZnSO_4$ electrolyte (Fig. 3g), mainly induced by the irreversible crystal structure changes. These results demonstrate the reversible changes in the valence state of V, interplanar spacing, and crystalline structure of the $NH_4V_4O_{10}$ cathode and verify the reversible (de) intercalation reaction of metal cations during the cycling process.[58]

However, determining the detailed reaction mechanism of the $NH_4V_4O_{10}$ cathode in the $ZnSO_4$–seawater electrolyte is challenging due to its complex composition. DFT calculations were further performed to explore the possible reactions between metal cations and the $NH_4V_4O_{10}$ cathode to address this dilemma. Firstly, the solvation energy of $Zn^{2+}$ ions (−13.92 eV) is stronger than that of alkali metal cations (Fig. 4a and S28†), indicating a relatively slower desolvation process for

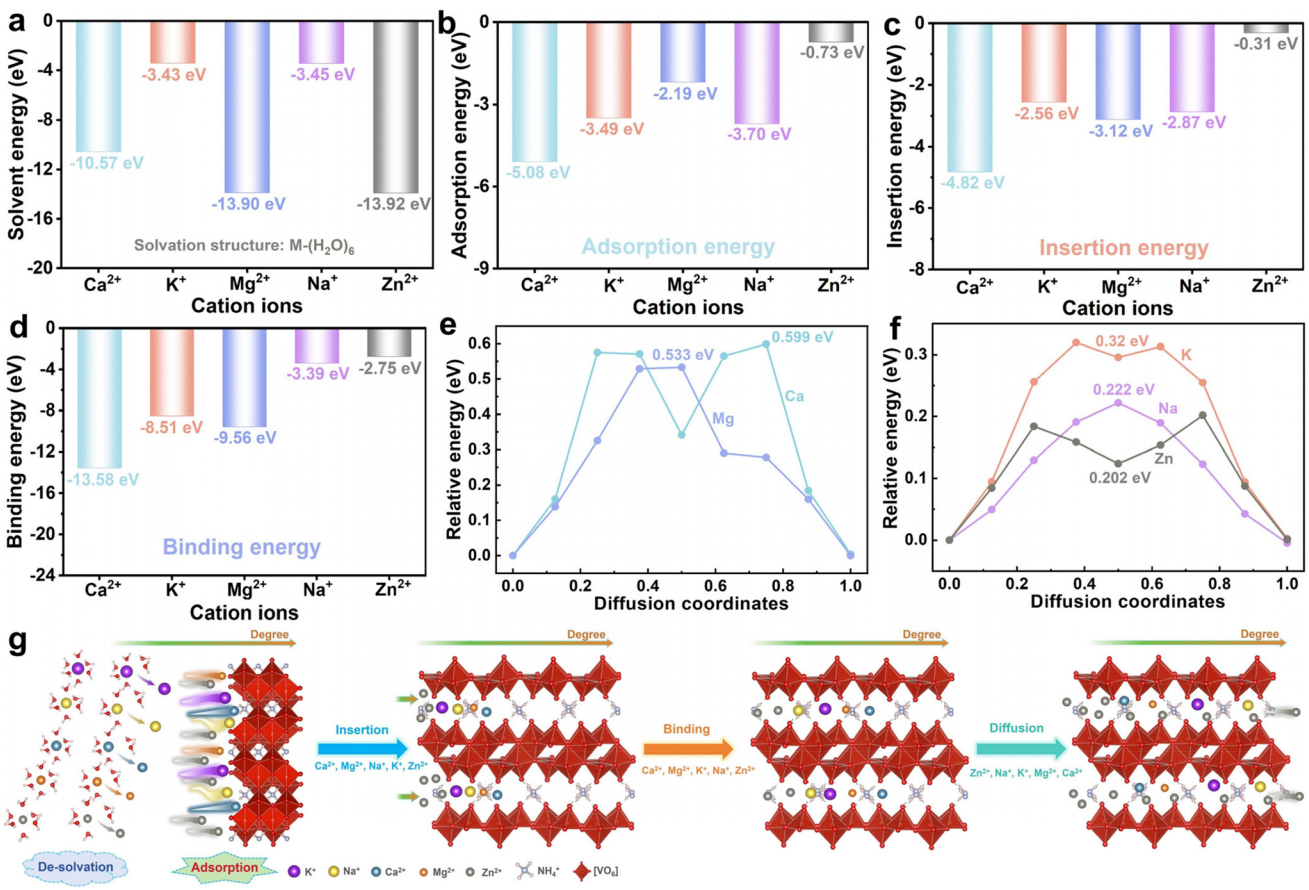


**Fig. 4** (a) Solvation energy, (b) adsorption energy, (c) insertion energy and (d) binding energy of different metal cations; (e and f) diffusion energy barriers of $Ca^{2+}$, $K^+$, $Mg^{2+}$, $Na^+$, and $Zn^{2+}$ ions in the crystal structure of $NH_4V_4O_{10}$; (g) schematic illustration of the reaction mechanism of the $NH_4V_4O_{10}$ cathode in the $ZnSO_4$–seawater electrolyte.

$Zn^{2+}$ ions. Secondly, the adsorption energy of metal cations on the surface of $NH_4V_4O_{10}$ is illustrated in Fig. 4b and S29.† The thermodynamic adsorption energies of $Ca^{2+}$, $K^+$, $Mg^{2+}$, and $Na^+$ ions are higher than that of $Zn^{2+}$ ions (−0.73 eV), suggesting a preferential adsorption behavior for alkali metal cations. Thirdly, Fig. 4c and S30† summarize the insertion energies between the metal cations and $NH_4V_4O_{10}$, and the insertion energies of the alkali metal cations are stronger than that of $Zn^{2+}$ ions. In general, the stronger the insertion energy, the greater the thermodynamic heat release and the easier the intercalation of metal ions in $NH_4V_4O_{10}$, manifesting the prioritized insertion of alkali metal cations under equal conditions. Fourthly, the binding energy between $Zn^{2+}$ ions and $NH_4V_4O_{10}$ is the lowest (Fig. 4d and S31†), whereas that between $Ca^{2+}$ ions and $NH_4V_4O_{10}$ is the highest (−13.58 eV). The weaker the binding energy, the more favorable the bulk diffusion of metal cations in the crystal structure of $NH_4V_4O_{10}$. In addition, the stronger the binding energy between the alkali metal cations and $NH_4V_4O_{10}$, the greater the damage to the structural stability of $NH_4V_4O_{10}$ caused by the (de)intercalation of alkali metal cations, which can explain the unstable cycling performance shown in Fig. S14.† Fifthly, the bulk diffusion energy barriers and diffusion paths of the metal cations in the crystal structure of $NH_4V_4O_{10}$ were investigated (Fig. 4e, f and S32†). The diffusion energy barriers of $Ca^{2+}$, $Mg^{2+}$, $K^+$, $Na^+$, and $Zn^{2+}$ ions are 0.599, 0.533, 0.32, 0.222, and 0.202 eV, respectively, demonstrating the fastest and slowest diffusion kinetics for $Ca^{2+}$ and $Zn^{2+}$ ions in $NH_4V_4O_{10}$, which agrees with the binding energy results shown in Fig. 4d.

Based on the above analyses, Fig. 4g depicts the detailed reaction process of metal cations in the crystal structure of the $NH_4V_4O_{10}$ cathode, consisting of five steps: interfacial desolvation, surface adsorption, bulk insertion, bulk binding, and bulk diffusion. Briefly, the introduction of alkali metal cations can effectively reduce the corresponding desolvation energy, and enhance the adsorption as well as insertion energy to facilitate the reaction kinetics of the $NH_4V_4O_{10}$ cathode.[59,60] To verify the universality of the seawater electrolyte, an α-$MnO_2$ cathode was successfully prepared (Fig. S33†) and its cycling performances in the $ZnSO_4$–seawater electrolyte were further analyzed (Fig. S34†). The reversible capacity of the α-$MnO_2$ cathode in the $ZnSO_4$ electrolyte is lower than that in the $ZnSO_4$–seawater electrolyte, indicating the positive contribution of the high-entropy electrolyte to both vanadium- and manganese-based cathodes.

## 3. Conclusion

In summary, natural seawater was used to configure high-entropy electrolytes for ZIBs, and its positive effects on the zinc metal anode and the $NH_4V_4O_{10}$ cathode were further demonstrated based on experimental data and theoretical calculations. With respect to the zinc metal anode, Zn//Zn cells in the seawater electrolyte exhibit a steady potential polarization at 5 mA $cm^{-2}$, a low activation energy barrier (27.43 kJ $mol^{-1}$), and a stable interfacial reaction environment (pH change: 4.92–5.16). In addition, Zn//Cu cells in the seawater electrolyte show a dendrite-free interface and a high plating/stripping CE of 99.13% at 2 mA $cm^{-2}$. With respect to the $NH_4V_4O_{10}$ cathode, the Zn//$NH_4V_4O_{10}$ cells in the seawater electrolyte yield a stable pH change (4.96–5.07), a low activation energy barrier (14.38 kJ $mol^{-1}$), a high capacity of 229.8 mA h $g^{-1}$ after 100 cycles at 0.5 A $g^{-1}$, and long-term cycling stability for 500 cycles at 2 A $g^{-1}$. These satisfactory results can be attributed to the low reduction potential, low desolvation energy, strong adsorption energy, and strong insertion energy of alkali metal cations, which effectively reduce the activation energy barriers and facilitate interfacial reaction kinetics. This study may drive the utilization of seawater resources, and promote the development of seawater-based secondary batteries.

## Author contributions

Chuancong Zhou: conceptualization, data curation, formal analysis, validation, investigation, visualization; Zhenming Xu: software, validation, visualization; Min Chen: methodology, data curation, writing – original draft; Qing Nan: investigation, formal analysis; Jie Zhang: resources, visualization; Yating Gao: validation, data curation; Zejun Zhao: conceptualization, methodology; Zhenyue Xing: formal analysis, visualization; Jing Li: resources, formal analysis; Peng Rao: methodology, funding acquisition; Zhenye Kang: supervision, funding acquisition; Xiaodong Shi: conceptualization, funding acquisition, supervision, project administration; Xinlong Tian: writing – review & editing, supervision, project administration.

## Data availability

The data that support the findings of this work are available within the article and the corresponding ESI.†

## Conflicts of interest

There are no conflicts of interest to declare.

## Acknowledgements

The authors thank the National Natural Science Foundation of China (52274297, 52164028 and 22309029), the Research Fund of the Innovation Platform for Academicians of Hainan Province (YSPTZX202315), the Collaborative Innovation Center of Marine Science and Technology of Hainan University (XTCX2022HYC14), and the Start-up Research Foundation of Hainan University (KYQD(ZR)-23069, 23169 and 20008). Additionally, the authors acknowledge the support for comprehensive characterization provided by the Pico Electron Microscopy Center of Hainan University, and this work is par-

tially supported by the High Performance Computing Platform of Nanjing University of Aeronautics and Astronautics.

## References

1 Y. Liu, X. Lu, F. Lai, T. Liu, P. R. Shearing, I. P. Parkin, G. He and D. J. Brett, Rechargeable aqueous Zn-based energy storage devices, *Joule*, 2021, **5**(11), 2845–2903.
2 C. Zhou, L. Shan, Q. Nan, J. Zhang, Z. Fan, B. Tang, J. Li, J. Yang, H. Zhang and Z. Kang, Construction of Robust Organic-Inorganic Interface Layer for Dendrite-Free and Durable Zinc Metal Anode, *Adv. Funct. Mater.*, 2024, 2312696.
3 R. Chen, C. Zhang, J. Li, Z. Du, F. Guo, W. Zhang, Y. Dai, W. Zong, X. Gao and J. Zhu, A hydrated deep eutectic electrolyte with finely-tuned solvation chemistry for high-performance zinc-ion batteries, *Energy Environ. Sci.*, 2023, **16**(6), 2540–2549.
4 Z. Liu, R. Wang, Y. Gao, S. Zhang, J. Wan, J. Mao, L. Zhang, H. Li, J. Hao and G. Li, Low-cost multi-function electrolyte additive enabling highly stable interfacial chemical environment for highly reversible aqueous zinc ion batteries, *Adv. Funct. Mater.*, 2023, **33**(49), 2308463.
5 J. Cao, D. Zhang, R. Chanajaree, Y. Yue, Z. Zeng, X. Zhang and J. Qin, Stabilizing zinc anode via a chelation and desolvation electrolyte additive, *Adv. Powder Mater.*, 2022, **1**(1), 100007.
6 S. Liu, R. Zhang, J. Mao, Y. Zhao, Q. Cai and Z. Guo, From room temperature to harsh temperature applications: Fundamentals and perspectives on electrolytes in zinc metal batteries, *Sci. Adv.*, 2022, **8**(12), eabn5097.
7 J. Li, D. Röhrens, G. Dalfollo, X. Wu, Z. Lu, Q. Gao, B. Han, R. Sun, C. Zhou and J. Wang, Low-temperature replacement construction of three-dimensional corrosion-resistant interface for deeply rechargeable Zn metal batteries, *Nano Mater. Sci.*, 2024, **6**(3), 329–336.
8 D. G. Vazquez, T. P. Pollard, J. Mars, J. M. Yoo, H.-G. Steinrück, S. E. Bone, O. V. Safonova, M. F. Toney, O. Borodin and M. R. Lukatskaya, Creating water-in-salt-like environment using coordinating anions in non-concentrated aqueous electrolytes for efficient Zn batteries, *Energy Environ. Sci.*, 2023, **16**(5), 1982–1991.
9 X. Xie, H. Fu, Y. Fang, B. Lu, J. Zhou and S. Liang, Manipulating ion concentration to boost two-electron $Mn^{4+}/Mn^{2+}$ redox kinetics through a colloid electrolyte for high-capacity zinc batteries, *Adv. Energy Mater.*, 2022, **12**(5), 2102393.
10 G. Li, Z. Zhao, S. Zhang, L. Sun, M. Li, J. A. Yuwono, J. Mao, J. Hao, J. Vongsvivut and L. Xing, A biocompatible electrolyte enables highly reversible Zn anode for zinc ion battery, *Nat. Commun.*, 2023, **14**(1), 6526.
11 Z. Xing, G. Xu, X. Xie, M. Chen, B. Lu, J. Zhou and S. Liang, Highly reversible zinc-ion battery enabled by suppressing vanadium dissolution through inorganic $Zn^{2+}$ conductor electrolyte, *Nano Energy*, 2021, **90**, 106621.
12 X. Tong, Y. Li, N. Pang, Y. Zhou, D. Wu, D. Xiong, S. Xu, L. Wang and P. K. Chu, Highly active cobalt-doped nickel sulfide porous nanocones for high-performance quasi-solid-state zinc-ion batteries, *J. Energy Chem.*, 2022, **66**, 237–249.
13 W. Wang, C. Li, S. Liu, J. Zhang, D. Zhang, J. Du, Q. Zhang and Y. Yao, Flexible Quasi-Solid-State Aqueous Zinc-Ion Batteries: Design Principles, Functionalization Strategies, and Applications, *Adv. Energy Mater.*, 2023, **13**(18), 2300250.
14 Y. Lv, Y. Xiao, L. Ma, C. Zhi and S. Chen, Recent advances in electrolytes for "beyond aqueous" zinc-ion batteries, *Adv. Mater.*, 2022, **34**(4), 2106409.
15 Y. Xu, X. Zhou, Z. Chen, Y. Hou, Y. You and J. Lu, Electrolyte formulas of aqueous zinc ion battery: A physical difference with chemical consequences, *Mater. Today*, 2023, **66**, 339–347.
16 C. Liu, Q. Li, Y. Lin, Z. Wei, Y. Yang, C. Han, M. Zhu, H. Zhang and H. Li, Functional group differentiation of isomeric solvents enables distinct zinc anode chemistry, *Nano Res. Energy*, 2023, **2**(2), e9120064.
17 Y. Shang and D. Kundu, A path forward for the translational development of aqueous zinc-ion batteries, *Joule*, 2023, **7**(2), 244–250.
18 C. Yang, X. Liu, Y. Lin, L. Yin, J. Lu and Y. You, Entropy-driven solvation towards low-temperature sodium-ion batteries with temperature-adaptive feature, *Adv. Mater.*, 2023, 2301817.
19 H. Zhang, Y. Wang, J. Huang, W. Li, X. Zeng, A. Jia, H. Peng, X. Zhang and W. Yang, Low-Enthalpy and High-Entropy Polymer Electrolytes for Li-Metal Battery, *Energy Environ. Mater.*, 2022, e12514.
20 Y. Zeng, B. Ouyang, J. Liu, Y.-W. Byeon, Z. Cai, L. J. Miara, Y. Wang and G. Ceder, High-entropy mechanism to boost ionic conductivity, *Science*, 2022, **378**(6626), 1320–1324.
21 Q. Wang, C. Zhao, J. Wang, Z. Yao, S. Wang, S. G. H. Kumar, S. Ganapathy, S. Eustace, X. Bai and B. Li, High entropy liquid electrolytes for lithium batteries, *Nat. Commun.*, 2023, **14**(1), 440.
22 Q. Wang, C. Zhao, Z. Yao, J. Wang, F. Wu, S. G. H. Kumar, S. Ganapathy, S. Eustace, X. Bai and B. Li, Entropy-driven liquid electrolytes for lithium batteries, *Adv. Mater.*, 2023, **35**(17), 2210677.
23 Z. Liu, X. Luo, L. Qin, G. Fang and S. Liang, Progress and prospect of low-temperature zinc metal batteries, *Adv. Powder Mater.*, 2022, **1**(2), 100011.
24 W. Zhang, H. Xia, Z. Zhu, Z. Lv, S. Cao, J. Wei, Y. Luo, Y. Xiao, L. Liu and X. Chen, Decimal solvent-based high-entropy electrolyte enabling the extended survival temperature of lithium-ion batteries to −130 °C, *CCS Chem.*, 2021, **3**(4), 1245–1255.
25 S. Wang, K. Wang, Y. Zhang, Y. Jie, X. Li, Y. Pan, X. Gao, Q. Nian, R. Cao and Q. Li, High-entropy Electrolyte Enables High Reversibility and Long Lifespan for Magnesium Metal Anodes, *Angew. Chem., Int. Ed.*, 2023, e202304411.
26 S. C. Kim, J. Wang, R. Xu, P. Zhang, Y. Chen, Z. Huang, Y. Yang, Z. Yu, S. T. Oyakhire, W. Zhang, *et al.*, High-

entropy electrolytes for practical lithium metal batteries, *Nat. Energy*, 2023, **8**(8), 814–826, DOI: 10.1038/s41560-023-01280-1.

27 C. Yang, J. Xia, C. Cui, T. P. Pollard, J. Vatamanu, A. Faraone, J. A. Dura, M. Tyagi, A. Kattan and E. Thimsen, All-temperature zinc batteries with high-entropy aqueous electrolyte, *Nat. Sustainability*, 2023, **6**(3), 325–335.

28 M. Qiu, P. Sun, K. Han, Z. Pang, J. Du, J. Li, J. Chen, Z. L. Wang and W. Mai, Tailoring water structure with high-tetrahedral-entropy for antifreezing electrolytes and energy storage at −80 °C, *Nat. Commun.*, 2023, **14**(1), 601.

29 J. Yu, C.-X. Zhao, J.-N. Liu, B.-Q. Li, C. Tang and Q. Zhang, Seawater-based electrolyte for Zinc-air batteries, *Green Chem. Eng.*, 2020, **1**(2), 117–123.

30 J. Yu, B.-Q. Li, C.-X. Zhao and Q. Zhang, Seawater electrolyte-based metal-air batteries: from strategies to applications, *Energy Environ. Sci.*, 2020, **13**(10), 3253–3268.

31 X. Guo, Z. Zhang, J. Li, N. Luo, G.-L. Chai, T. S. Miller, F. Lai, P. Shearing, D. J. Brett and D. Han, Alleviation of dendrite formation on zinc anodes via electrolyte additives, *ACS Energy Lett.*, 2021, **6**(2), 395–403.

32 F. Wan, L. Zhang, X. Dai, X. Wang, Z. Niu and J. Chen, Aqueous rechargeable zinc/sodium vanadate batteries with enhanced performance from simultaneous insertion of dual carriers, *Nat. Commun.*, 2018, **9**(1), 1656.

33 P. Wang, X. Xie, Z. Xing, X. Chen, G. Fang, B. Lu, J. Zhou, S. Liang and H. J. Fan, Mechanistic Insights of $Mg^{2+}$-Electrolyte Additive for High-Energy and Long-Life Zinc-Ion Hybrid Capacitors, *Adv. Energy Mater.*, 2021, **11**(30), 2101158.

34 F. Ding, W. Xu, G. L. Graff, J. Zhang, M. L. Sushko, X. Chen, Y. Shao, M. H. Engelhard, Z. Nie and J. Xiao, Dendrite-free lithium deposition via self-healing electrostatic shield mechanism, *J. Am. Chem. Soc.*, 2013, **135**(11), 4450–4456.

35 Z. Hu, F. Zhang, Y. Zhao, H. Wang, Y. Huang, F. Wu, R. Chen and L. Li, A Self-Regulated Electrostatic Shielding Layer toward Dendrite-Free Zn Batteries, *Adv. Mater.*, 2022, **34**(37), 2203104.

36 R. Zhao, H. Wang, H. Du, Y. Yang, Z. Gao, L. Qie and Y. Huang, Lanthanum nitrate as aqueous electrolyte additive for favourable zinc metal electrodeposition, *Nat. Commun.*, 2022, **13**(1), 3252.

37 Y. Ding, X. Zhang, T. Wang, B. Lu, Z. Zeng, Y. Tang, J. Zhou and S. Liang, A dynamic electrostatic shielding layer toward highly reversible Zn metal anode, *Energy Storage Mater.*, 2023, 102949.

38 Y. Yang, G. Qu, H. Wei, Z. Wei, C. Liu, Y. Lin, X. Li, C. Han, C. Zhi and H. Li, Weakly solvating effect spawning reliable interfacial chemistry for aqueous Zn/Na hybrid batteries, *Adv. Energy Mater.*, 2023, **13**(12), 2203729.

39 Z. Liu, Q. Yang, D. Wang, G. Liang, Y. Zhu, F. Mo, Z. Huang, X. Li, L. Ma and T. Tang, A flexible solid-state aqueous zinc hybrid battery with flat and high-voltage discharge plateau, *Adv. Energy Mater.*, 2019, **9**(46), 1902473.

40 H. He, D. Luo, L. Zeng, J. He, X. Li, H. Yu and C. Zhang, 3D printing of fast kinetics reconciled ultra-thick cathodes for high areal energy density aqueous Li-Zn hybrid battery, *Sci. Bull.*, 2022, **67**(12), 1253–1263.

41 H. Tian, Z. Li, G. Feng, Z. Yang, D. Fox, M. Wang, H. Zhou, L. Zhai, A. Kushima and Y. Du, Stable, high-performance, dendrite-free, seawater-based aqueous batteries, *Nat. Commun.*, 2021, **12**(1), 237.

42 W. Zhang, W. Chen, X. Zhao, Q. Dang, Y. Li, T. Shen, F. Wu, L. Tang, H. Jiang and M. Hu, An Auto-Switchable Dual-Mode Seawater Energy Extraction System Enabled by Metal-Organic Frameworks, *Angew. Chem., Int. Ed.*, 2019, **58**(22), 7431–7434.

43 X. Xie, S. Liang, J. Gao, S. Guo, J. Guo, C. Wang, G. Xu, X. Wu, G. Chen and J. Zhou, Manipulating the ion-transfer kinetics and interface stability for high-performance zinc metal anodes, *Energy Environ. Sci.*, 2020, **13**(2), 503–510.

44 J. Zhu, Z. Bie, X. Cai, Z. Jiao, Z. Wang, J. Tao, W. Song and H. J. Fan, A Molecular-Sieve Electrolyte Membrane enables Separator-Free Zinc Batteries with Ultralong Cycle Life, *Adv. Mater.*, 2022, **34**(43), 2207209.

45 Q. Zhu, G. Sun, S. Qiao, D. Wang, Z. Cui, W. Zhang and J. Liu, Selective Shielding of the (002) Plane Enabling Vertically Oriented Zinc Plating for Dendrite-Free Zinc Anode, *Adv. Mater.*, 2023, 2308577.

46 Y. Wang, Q. Li, H. Hong, S. Yang, R. Zhang, X. Wang, X. Jin, B. Xiong, S. Bai and C. Zhi, Lean-water hydrogel electrolyte for zinc ion batteries, *Nat. Commun.*, 2023, **14**(1), 3890.

47 M. Liu, W. Yuan, G. Ma, K. Qiu, X. Nie, Y. Liu, S. Shen and N. Zhang, *In situ* Integration of a Hydrophobic and Fast-$Zn^{2+}$-Conductive Inorganic Interphase to Stabilize Zn Metal Anodes, *Angew. Chem., Int. Ed.*, 2023, e202304444.

48 M. Liu, L. Yao, Y. Ji, M. Zhang, Y. Gan, Y. Cai, H. Li, W. Zhao, Y. Zhao and Z. Zou, Nanoscale ultrafine zinc metal anodes for high stability aqueous zinc ion batteries, *Nano Lett.*, 2023, **23**(2), 541–549.

49 Z. Liu, Z. Guo, L. Fan, C. Zhao, A. Chen, M. Wang, M. Li, X. Lu, J. Zhang and Y. Zhang, Construct Robust Epitaxial Growth of (101) Textured Zinc Metal Anode for Long Life and High Capacity in Mild Aqueous Zinc-Ion Batteries, *Adv. Mater.*, 2023, 2305988.

50 Y. Zhao, C. Yang and Y. Yu, A review on covalent organic frameworks for rechargeable zinc-ion batteries, *Chin. Chem. Lett.*, 2023, 108865.

51 Z. Xing, Y. Sun, X. Xie, Y. Tang, G. Xu, J. Han, B. Lu, S. Liang, G. Chen and J. Zhou, Zincophilic electrode interphase with appended proton reservoir ability stabilizes Zn metal anodes, *Angew. Chem.*, 2023, **135**(5), e202215324.

52 T. Wang, Y. Tang, M. Yu, B. Lu, X. Zhang and J. Zhou, Spirally Grown Zinc-Cobalt Alloy Layer Enables Highly Reversible Zinc Metal Anodes, *Adv. Funct. Mater.*, 2023, 2306101.

53 W. Zhang, Y. Dai, R. Chen, Z. Xu, J. Li, W. Zong, H. Li, Z. Li, Z. Zhang and J. Zhu, Highly reversible zinc metal anode in a dilute aqueous electrolyte enabled by a pH buffer additive, *Angew. Chem., Int. Ed.*, 2023, **62**(5), e202212695.

54 X. Yu, Z. Li, X. Wu, H. Zhang, Q. Zhao, H. Liang, H. Wang, D. Chao, F. Wang and Y. Qiao, Ten concerns of Zn metal anode for rechargeable aqueous zinc batteries, *Joule*, 2023, **7**(6), 1145–1175.

55 S. Li, X. Xu, W. Chen, J. Zhao, K. Wang, J. Shen, X. Chen, X. Lu, X. Jiao and Y. Liu, Synergetic impact of oxygen and vanadium defects endows $NH_4V_4O_{10}$ cathode with superior performances for aqueous zinc-ion battery, *Energy Storage Mater.*, 2023, 103108.

56 X. Shi, C. Zhou, Y. Gao, J. Yang, Y. Xie, S. Feng, J. Zhang, J. Li, X. Tian and H. Zhang, Pore structure and oxygen content design of amorphous carbon toward a durable anode for potassium/sodium-ion batteries, *Carbon Energy*, 2024, e534.

57 B. Tang, J. Zhou, G. Fang, F. Liu, C. Zhu, C. Wang, A. Pan and S. Liang, Engineering the interplanar spacing of ammonium vanadates as a high-performance aqueous zinc-ion battery cathode, *J. Mater. Chem. A*, 2019, **7**(3), 940–945.

58 Z. Liu, L. Qin, X. Cao, J. Zhou, A. Pan, G. Fang, S. Wang and S. Liang, Ion migration and defect effect of electrode materials in multivalent-ion batteries, *Prog. Mater. Sci.*, 2022, **125**, 100911.

59 X. Wang, Y. Wang, A. Naveed, G. Li, H. Zhang, Y. Zhou, A. Dou, M. Su, Y. Liu and R. Guo, Magnesium Ion Doping and Micro-Structural Engineering Assist $NH_4V_4O_{10}$ as a High-Performance Aqueous Zinc Ion Battery Cathode, *Adv. Funct. Mater.*, 2023, **33**(48), 2306205.

60 X. Ma, X. Cao, M. Yao, L. Shan, X. Shi, G. Fang, A. Pan, B. Lu, J. Zhou and S. Liang, Organic-inorganic hybrid cathode with dual energy-storage mechanism for ultrahigh-rate and ultralong-life aqueous zinc-ion batteries, *Adv. Mater.*, 2022, **34**(6), 2105452.